

Kinematic, finite strain and vorticity analysis of the Sisters Shear Zone, Stewart Island, New Zealand



Uwe Ring^{a, *}, Matthias Bernet^b, Andy Tulloch^c

^a Department of Geological Sciences, Stockholm University, 10691 Stockholm, Sweden

^b Institut des Sciences de la Terre, Université Joseph Fourier, 38041 Grenoble Cedex, France

^c GNS Science, Dunedin, New Zealand

ARTICLE INFO

Article history:

Received 25 November 2014

Received in revised form

11 February 2015

Accepted 13 February 2015

Available online 21 February 2015

Keywords:

Shear zone

Structural analysis

Kinematic vorticity

Finite strain

Extensional deformation

New Zealand

ABSTRACT

The Sisters Shear Zone (SSZ) on Stewart Island, New Zealand, is a greenschist-facies extensional shear zone active prior to and possibly during the development of the Pacific–Antarctica spreading ridge at ~76 Ma. We report quantitative kinematic and rotation data as well as apatite fission-track (AFT) ages from the SSZ. Early kinematic indicators associated with the NNE-trending stretching lineation formed under upper greenschist-facies metamorphism and show alternating top-to-the-NNW and top-to-the-SSE senses of shear. During progressive exhumation lowermost greenschist-facies and brittle-ductile kinematic indicators depict a more uniform top-to-the-SSE sense of shear in the topmost SSZ just below the detachment plane. Deformed metagranites in the SSZ allow the reconstruction of deformation and flow parameters. The mean kinematic vorticity number (W_m) ranges from 0.10 to 0.89; smaller numbers prevail in the deeper parts of the shear zone with a higher degree of simple shear deformation in the upper parts of the shear zone (deeper and upper parts relate to present geometry). High finite strain intensity correlates with low W_m and high W_m numbers near the detachment correlate with relatively weak strain intensity. Finite strain shows oblate geometries. Overall, our data indicate vertical and possibly temporal variations in deformation of the SSZ. Most AFT ages cluster around 85–75 Ma. We interpret the AFT ages to reflect the final stages of continental break-up just before and possibly during the initiation of sea-floor spreading between New Zealand and Antarctica.

© 2015 Elsevier Ltd. All rights reserved.

1. Introduction

1.1. Extensional shear zones

Shear zones are arguably the most important deformation structures in the lithosphere. They are the most spectacular expression of the heterogeneity of deformation at all scales. In regions of lithospheric extension shear zones can accommodate tens or hundreds of kilometres of displacement (Foster and John, 1999; Wells et al., 2000; Ring et al., 2001; Thomson and Ring, 2006). Large-scale extension is commonly expressed by the development of metamorphic core complexes (Lister and Davis, 1989), which tectonically separate a mid/lower crustal core in the lower plate from non-metamorphosed sediments in the upper plate. The displacement is usually concentrated into a few tens to a few

hundreds of meters thick ductile shear zone at the top of the exhuming metamorphic core. This ductile shear zone is overlain by a brittle detachment fault.

Ramsay and Graham (1970) advocated a model of progressive simple shear for ductile shear zones. Quantitative studies over the last two decades have shown that the deformation in shear zones is more complex and usually involves a coaxial component (Simpson and De Paor, 1993; Northrup et al., 1996; Grasemann et al., 1999; Ring, 1999; Kumerics et al., 2005; Bailey et al., 2007; Ring and Kumerics, 2008). In extensional terrains this pure-shear component is expressed by subvertical coaxial shortening leading to elongating shear zones (stretching faults in the sense of Means, 1989). Sullivan (2008) showed that strain intensity and strain geometry varies very significantly parallel to the tectonic transport direction in the Raft River low-angle extensional shear zone in the Basin and Range province. What is less well investigated are vertical and temporal variations in deformation (strain, rotation, translation) in shallow-dipping extensional shear zones.

* Corresponding author.

1.2. Metamorphic core complexes in New Zealand

The metamorphic core complexes on the west and south coast of the South Island of New Zealand are generally interpreted as precursors of late Cretaceous Tasman Sea and Southern Ocean rifting (Tulloch and Kimbrough, 1989; Gaina et al., 1998). The most prominent of the New Zealand core complexes is the Paparoa core complex (Fig. 1), which had a major phase of extensional faulting at ~115–110 Ma when the upper amphibolite-facies, in part migmatitic, footwall cooled at rates of ~100 °C Myr⁻¹ (Spell et al., 2000; Schulte et al., 2014). The Paparoa core complex is a bivergent core complex characterized by two oppositely dipping and displacing

detachments. Modelling work by Gessner et al. (2007) suggests that a bivergent symmetry develops when the lower crust is hot and has a low viscosity during extension and there is a pronounced strength difference between the upper and lower crust. A monovergent core complex, i.e. one that is characterized by a single shear zone/detachment system, develops when the viscosity contrasts between upper and lower crust are less, i.e. the mid/lower crust is stronger. These core complexes usually expose greenschist-facies rocks in their metamorphic core.

Another metamorphic core complex in New Zealand is the Pegasus core complex on Stewart Island (Fig. 2) (Kula et al., 2009). The overall geometry of the Pegasus core complex is not well

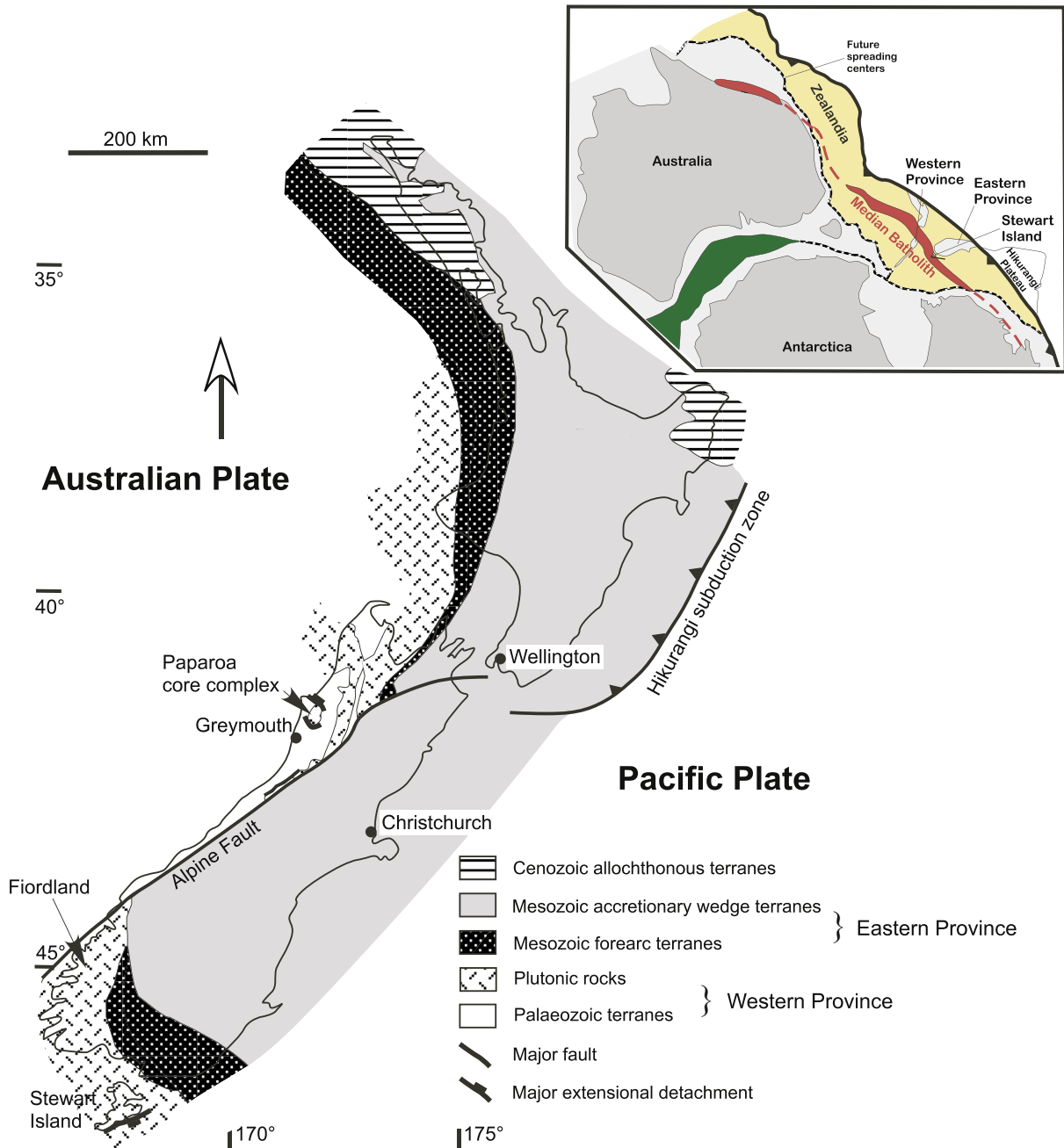


Fig. 1. Simplified terrane map of New Zealand and location of Stewart Island, the latter being made up by plutonic rocks of the Western Province; also shown is Paparoa core complex (inset shows mid Cretaceous subduction system at the eastern margin of Gondwana with Median Batholith magmatic arc; the future South Island of New Zealand is represented in this sketch by Eastern Province and small sliver of Western Province).

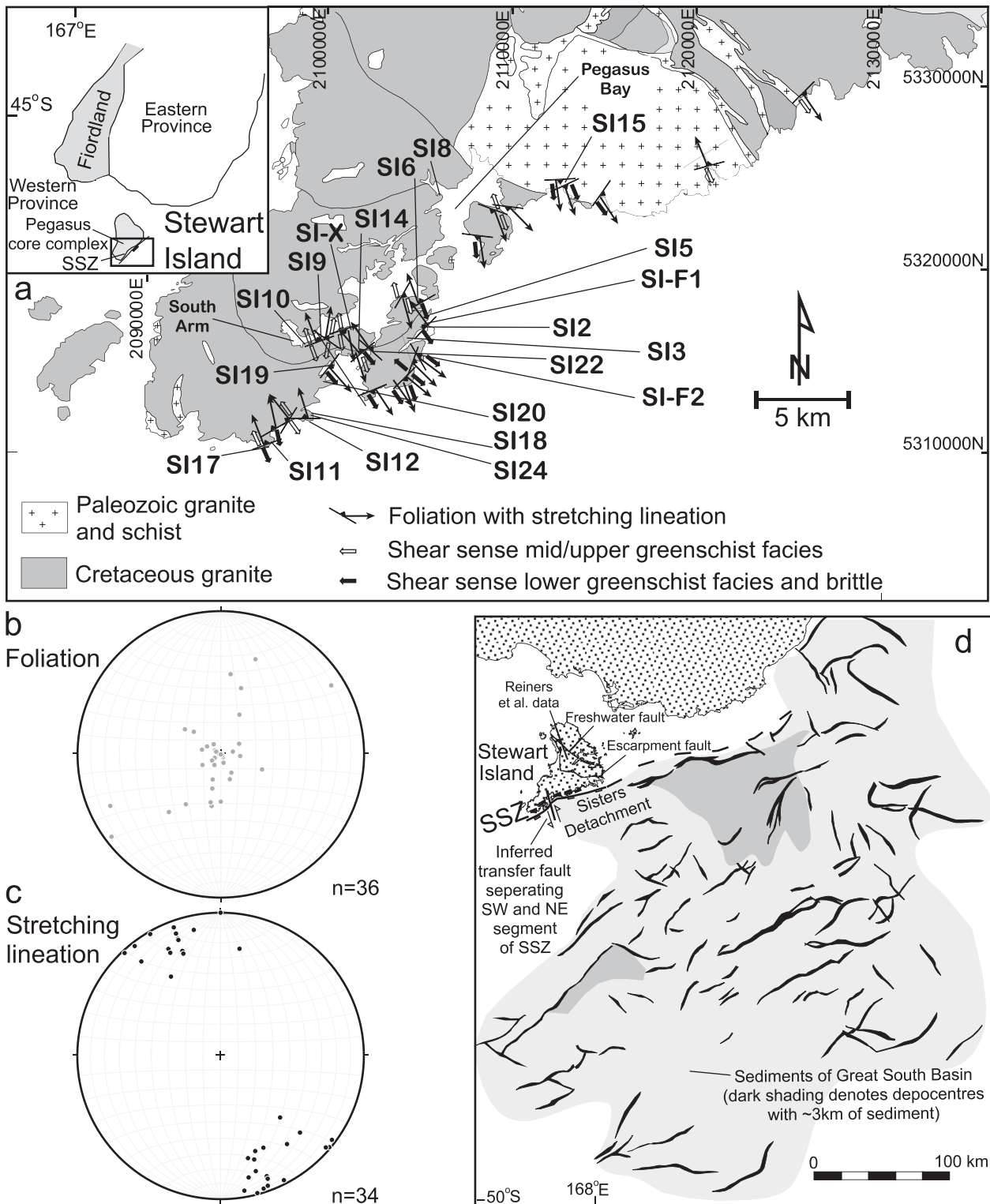


Fig. 2. (a) Structural map of the SSZ, shown are strike and dip of mylonitic foliation and trend of stretching lineation (arrow heads point down plunge), also shown is sense of shear for upper/mid greenschist-facies deformation (basically defined in field by stability of biotite) and lower greenschist-facies shearing. Sample localities shown as well. Inset: location of Stewart Island, Pegasus core complex and Sisters Shear Zone. (b) Poles to foliation planes, lower hemisphere projection. (c) Stretching lineation data, lower hemisphere projection. (d) Stewart Island, trace of Sisters Detachment and Great South Basin (modified from Kula et al., 2009). Note that basin architecture in Great South Basin is characterized by two orthogonal sets of normal faults. Also shown are early Cretaceous thrusts and locality of Reiners et al. (2004) study.

known. Kula et al. (2009) reported along-strike differences in the kinematics of the Sister Shear Zone (SSZ), which is separating the Pegasus core complex from overlying sediments of the Great South Basin (Fig. 2). The southwest part of the SSZ is supposed to have a

top-N displacement that is thought to be associated with a hypothetical top-S shear zone giving the structure an overall bivergent symmetry. The northeast part of the SSZ is supposed to be a monovergent top-S shear zone (Kula et al., 2009, their Figs. 2 and

11). In some respect this interpretation suggests that the Pegasus core complex has a mixed symmetry, i.e. bivergent symmetry in the SW and monovergent symmetry in the NE. Kula et al. (2009) did not report any quantitative structural data to support their along-strike differences in shear zone kinematics and overall geometry. Muscovite, biotite and feldspar $^{40}\text{Ar}/^{39}\text{Ar}$ by Kula et al. (2009) suggest that footwall cooling started at ~94 Ma with accelerated cooling between 89 and 82 Ma.

We report the results of a kinematic, strain and rotation analyses from the SSZ for further constraining its kinematics and geometry. Our results suggest that top-to-the-SSE and top-to-the-NNW shear sense indicators resulted from a relatively high degree of coaxial deformation with the pure/simple shear ratio increasing downwards in the SSZ. Our data do not support a model in which the kinematics of the shear zone changed along strike.

2. Setting

The Mesozoic geology of New Zealand was dominated by a long-lived subduction zone at the eastern margin of Gondwana (Fig. 1). In this subduction complex an Eastern and a Western province are distinguished. The forearc terranes of the Eastern Province are mostly trench-fill sediments. The Western Province is made up by the subduction-related magmatic arc (Median Batholith) and its surrounding rocks (Mortimer, 2004).

At about 110 Ma the subduction system was shut off and the New Zealand continent underwent a major phase of extensional tectonism. Initially extension was manifested by the development of core complexes, which developed within the thermally softened lithosphere of the Western Province. The magmatic arc of the subduction zone developed within high-grade gneisses, Paleozoic arc-related granitoids and low-grade Ordovician sedimentary rocks (Tulloch and Kimbrough, 1989; Rattenbury, 1991; Nathan et al., 2002). Mid Cretaceous extensional structures in the Eastern Province are graben structures bounded by high-angle normal faults recording very limited horizontal extension (Mortimer, 1993; Deckert et al., 2002). This core complex/graben stage was followed by the opening of the Tasman Sea at ~83 Ma and later the Southern Ocean basin at ~76 Ma (Gaina et al., 1998).

Stewart Island represents the southeastern continuation of the Median Batholith (Allibone and Tulloch, 1997) (Fig. 2). Allibone and Tulloch (1997, 2004) showed that basement rocks making up Stewart Island are mainly granites of various compositions and ages. Intrusion ages range from late Paleozoic through Mesozoic marking four pulses of magmatism during the Carboniferous (345–290 Ma), Jurassic (170–165 Ma), latest Jurassic to earliest Cretaceous (151–128 Ma), and early/mid Cretaceous (128–100 Ma) (Allibone and Tulloch, 2004).

Structures present on the island include the Freshwater and Escarpment faults, and the Gutter shear zone, all of which are NW-striking thrusts that accommodated dextral transpressive early Cretaceous intra-arc shortening (Allibone and Tulloch, 2004, 2008). The SSZ is a NE-striking low-angle extensional shear zone running along the southeastern edge of Stewart Island (Fig. 2) (Allibone and Tulloch, 2008; Kula et al., 2009). The rocks in the shear zone are granitoids variably deformed that include breccia, protomylonite, mylonite, and ultramylonite (Kula et al., 2009). Stewart Island itself can largely be regarded as the updomed footwall, i.e. the Pegasus core complex. The top of the SSZ is the Sisters Detachment, the latter of which is overlain by sediments of the Great South Basin (Fig. 2d).

The SSZ dips gently (15–35°) to the SE. Kula et al. (2009) suggested that the SSZ is made up by NE and SW segments separated by a left-lateral transfer fault (Fig. 2d). Tulloch et al. (2006) proposed that the SSZ is an about 400–500 km long crustal to

lithospheric scale structure that underlies and controlled the formation of the Great South Basin, a view that has been adopted by Uruski and Ilg (2006) for interpreting seismic data from the Great South Basin. The latter formed between 100 and 84 Ma and accumulated up to 3 km of sediment during that time span (Uruski and Ilg, 2006). The basin architecture is dominated by two sets of normal faults striking NE and NW (Fig. 2d).

3. Methods

3.1. Finite strain analysis

To describe finite strain in a rock six independent variables are required. Three variables describe the orientation of the principal stretching directions X, Y and Z, where $X \geq Y \geq Z$. The remaining three variables describe the magnitude of the principal strain along these directions, which are represented by the absolute principal stretches S_X , S_Y and S_Z ($S_X \geq S_Y \geq S_Z$). The stretches are defined by l_f/l_i , where l_i and l_f are the initial and final lengths of a material line. For practical purposes usually the principal axial ratios R_{XY} , R_{XZ} and R_{YZ} are used to describe strain, where $R_{XY} = S_X/S_Y$, $R_{XZ} = S_X/S_Z$ and $R_{YZ} = S_Y/S_Z$. For our calculations we assume constant volume deformation.

To quantify finite strain, the Fry method (Fry, 1979; Ramsay and Huber, 1983) was applied to 17 augengneiss samples from the SSZ (Fig. 2a). The Fry method provides a graphic solution to the center-to-center method. The basic principle of the latter is that the distances between the centers of objects are systematically related to the orientation of the finite-strain ellipsoid. The Fry strains are thought to represent the matrix strain (Ramsay and Huber, 1983; Ring, 1998; Kassem and Ring, 2004). Two-dimensional strain measurements were made on XZ and YZ sections in order to estimate the three-dimensional strain geometry. For Fry analysis, the central points of usually more than 100 feldspar grains per section were used to calculate strain. The strain estimates were used to calculate the finite-strain ellipsoid according to the modified least-square technique of Owens (1984). From the finite-strain data we calculated strain intensity, $d = \sqrt{(R_{XY}-1)^2 + (R_{YZ}-1)^2}$ and strain symmetry, $K = (R_{XY}-1)/(R_{YZ}-1)$.

3.2. Vorticity analysis

The foliation outside the shear zone is gently inclined relative to the shear-zone boundary suggesting a component of coaxial flattening which acted subperpendicular to the shear-zone walls. Grain shapes of quartz and feldspar have oblate geometries, which become, especially for quartz, more pronounced in the center of the shear zone. These observations qualitatively suggest that the degree of noncoaxiality, as expressed by the mean kinematic vorticity number, W_m , (Passchier, 1987, 1988) is lower than 1. Law et al. (2004, 2013) showed that at $W_m = 0.71$ the simple- ($W_m = 1$) and pure-shear ($W_m = 0$) component of deformation is equal.

To quantify the degree of noncoaxiality we used the rotation of porphyroclasts (Jeffery, 1922; Ghosh and Ramberg, 1976; Passchier, 1987; Simpson and De Paor, 1993). Two methods are used here: (1) the porphyroclast aspect ratio method (PAR) (Passchier, 1987) for samples that do not have many well developed shear-sense indicators and (2) the porphyroclast hyperbolic distribution method (PHD) (Simpson and De Paor, 1993) for samples with good shear-sense indicators. The main assumptions behind these techniques of vorticity estimation are perfect coupling between clast and matrix, no interference between adjacent clasts, 2D clast shapes and homogeneous, steady-state deformation (Xypolias, 2010).

(1) In a general shear-flow regime, particles with an aspect ratio above a critical value will rotate until they reach a stable orientation whereas particles below this critical value will rotate without ever finding a stable orientation. According to [Passchier \(1987\)](#), the value of this critical aspect ratio, R_c , is a function of W_m only, and is expressed by:

$$W_m = (R_c^2 - 1) / (R_c^2 + 1).$$

(2) The PHD method is also based on the rotational behaviour of rigid elliptical objects within an actively flowing matrix ([Simpson and De Paor, 1993, 1997](#)). The aspect ratio of porphyroclasts (R), and the orientation of their long axes with respect to a fixed reference frame (φ) is plotted in polar coordinates in a hyperbolic net. The shear zone boundary and its normal are used as a reference frame. Forward and backward rotating porphyroclasts define two fields that can be separated by a hyperbola. The cosine of the opening angle of the hyperbola defines W_m ([Xypolias, 2010](#)).

[Platt and Vissers \(1980\)](#) proposed a possible association of shear bands with the directions of minimum and maximum angular velocities of material lines in general flow. Synthetic shear bands rotate slowly toward the flow plane remaining active longer than high-angle antithetic shear bands that rotate rapidly and become inactive. The largest recorded angle between the synthetic shear bands and the shear plane is equal to half of the angle between the flow apophyses and the cosine of this angle provides an estimate of W_m ([Kurz and Northrup, 2008; Sullivan, 2008](#)). In two cases (SI9 and SI10) we used this technique to check the results of the PHD analysis.

3.3. Fission-track analysis

Fission-track (FT) analysis was carried out on 23 apatite samples to determine the cooling history of the SSZ footwall. We also analysed zircon but zircons were metamict resulting in very poorly defined ages, which are not being used herein. Apatite grains were separated from bulk samples using standard heavy mineral separation techniques. Apatites were mounted in epoxy, polished and etched for 20 s in 5.5 M HNO_3 at 21 °C. Randomly selected apatite and zircon grains of all samples were dated with the external detector method, using Durango and Fish-Canyon Tuff age standards, together with IRMM540 glass standards (15 ppm uranium) as neutron fluence monitors during irradiation at the Saclay Research Reactor, Gif-sur-Yvette, France. Mica detectors were etched for 18 min in 48% HF at 20 °C. FT ages were calculated with the BINOMFIT program of Brandon, as described in [Ehlers \(2005\)](#), using a zeta calibration factor ([Hurford and Green, 1983](#)) of 290.9 ± 14.5 for apatite. All samples were counted dry with a BH-2 Olympus microscope and FTStage 4 automated system at 1250× magnification at the fission-track laboratory at the Institut des Sciences de la Terre in Grenoble, France.

For apatite of typical Durango composition (0.4 wt% Cl) experimental and borehole data ([Green et al., 1989; Ketcham et al., 1999](#)) show that over geologic time tracks begin to anneal at temperatures above ca. 60 °C at a sufficient rate to be measurable, with complete annealing and total resetting of the apatite FT age occurring between 100 °C and 120 °C. This range (60–120 °C) of temperatures is labelled the apatite FT partial annealing zone. For samples that have undergone moderate to fast cooling at rates of 10–40 °C Myr^{-1} , a closure temperature of 110 ± 10 °C can be reasonably assumed for the most common apatite compositions (e.g. [Brandon et al., 1998; Ketcham et al., 1999](#)). In this study we use Dpar, the size of the fission-track etch pit parallel to the crystallographic c-axis, as a kinematic parameter for t-T modelling (see below) in lieu of Cl content measurements ([Donelick et al., 2005](#)).

The Dpar value is positively correlated with Cl content in apatite, but it is not a proxy for the chemical composition of the analysed grains. Apatites with Dpar values < 1.75 μm are considered as fast annealing and at lower temperatures (~60–120 °C), whereas Dpar values > 1.75 μm generally indicate slow annealing and at higher temperatures (~90–150 °C).

3.4. Thermal history modelling

A tool for testing geological models of t-T evolution against a thermochronological data set is provided by the computer code HeFTy (v.1.8.3; [Ketcham, 2005; Ketcham et al., 2007, 2009](#)). In HeFTy known FT annealing kinetics and He diffusion behaviour of apatite and zircon are considered. With HeFTy cooling and reheating scenarios can be tested against observed thermochronological data by forward and inverse modelling for determining possible t-T paths. Information on the geological evolution of an area can be implemented as t-T constraints. The program defines envelopes of good and acceptable results in t-T space that contain all paths passing baseline statistical criteria and that conform to user-entered geological constraints (for details see [Ketcham, 2009; Ketcham et al., 2009](#)). To compute FT annealing and He diffusion several calibration models are implemented in HeFTy (e.g. [Ketcham et al., 2007; Farley, 2000; Reiners et al., 2004; Wolf et al., 1996](#)). For this study AFT data (single grain apparent cooling ages, c-axes corrected confined track lengths distributions and Dpar) were run using the [Ketcham et al. \(2007\)](#) annealing model. For the model runs 100,000 Monte Carlo model t-T paths were tried.

4. Structures in the SSZ

We describe the structures in the SSZ from bottom to top. The deeper, higher-grade deformation fabrics are exposed in Pegasus Bay, especially well around South Arm, whereas higher parts of the shear zone with lower greenschist-facies structures are preferentially exposed along the coast of SE Stewart Island ([Fig. 2](#)).

Overall, the various granites in the SSZ show the typical heterogeneous deformation of metagranites with tens of meters thick mylonitic to ultramylonitic zones alternating with much thicker intervals depicting weak deformation and in part undeformed granite (see also [Kula et al., 2009](#)). In mylonitic zones, the foliation is defined by grain shape orientation of elongate feldspar crystals, ribbon quartz, polycrystalline quartz aggregates and strongly preferred alignment of white mica and biotite. In ultramylonite, the matrix is composed of ultra fine-grained black bands surrounding rounded feldspar porphyroclasts ([Fig. 3a, Fig. 4a–f](#)). The black bands are composed of quartz, feldspar and mica. The black colour is a function of the ultra fine grain size. The feldspar porphyroclasts are either aligned parallel to the foliation or have their long axes oriented at various angles to the penetrative foliation ([Fig. 3a](#)) (see also [Kula et al., 2009](#)).

There is a strong NNW-SSE trending stretching lineation on the mylonitic/ultramylonitic foliation planes ([Fig. 2](#)). The stretching lineation is expressed by the preferred orientation of quartz-feldspar aggregates, and white mica and biotite preferred orientation. Shear sense indicators associated with the stretching lineation are σ - and δ -type feldspar porphyroclasts, S-C fabrics, shear bands, flanking structures and mica fish ([Fig. 4](#)). These kinematic indicators formed within the stability field of biotite and white mica and quartz recrystallized in strain shadows and shear bands, and feldspar shows undulatory extinction and brittle fracturing, and rarely incipient dynamic recrystallization. The kinematic indicators yielded alternating top-to-the-SSE (37 out of 63) and top-to-the-NNW (26 out of 63) senses of shear with no obvious geographic pattern ([Fig. 2](#)).



Fig. 3. Field and hand specimen photographs of deformed rocks from SSZ; SSE in all photos to left. (a) Fine-grained, blackish ultramylonite, South Arm. Long axes of feldspar porphyroclasts plunge to the SSE and NNW; asymmetric tails of porphyroclasts provide top-to-the-SSE and top-to-the-NNW shear senses, XZ section ($S47^{\circ}14'36''$, $E167^{\circ}34'06''$). (b) Relatively steep NNW-dipping shear bands provide top-to-the-NNW sense of shear ($S47^{\circ}14'30''$, $E167^{\circ}39'00''$). (c) Cataclastically deformed chlorite-rich metagranite; P foliations and Riedel shear provide top-to-the-SSE shear sense ($S47^{\circ}10'55''$, $E167^{\circ}47'34''$). (d) S-dipping normal faults in metagranite ($S47^{\circ}14'30''$, $E167^{\circ}38'59''$).

Along the coast of southern Stewart Island, shear-zone related deformation becomes more localized and synkinematic mineralogy is consistent with lowermost greenschist-facies (Fig. 4g,h), mixed brittle-ductile (Fig. 3c) and brittle deformation (Fig. 3d). Quartz still mainly deforms ductilely expressed by oblique fabrics of dynamically recrystallized grains. Biotite is commonly strongly chloritized and feldspar shows brittle deformation (Fig. 4) such as cracks, cleavage fractures, kink bands and rotation along microfaults. These low-temperature deformation features also occur inland and overprint the higher temperatures fabrics described above. However, further inland they only occur locally whereas along most of the coastline the low-temperature deformation fabrics are penetrative.

The low-temperature deformation fabrics show the same geometrical patterns as the higher-grade ones. Shear bands associated with the retrograde stretching lineation exhibit pronounced chloritization of biotite. Feldspar porphyroclasts are severely sericitized. The asymmetry of retrograde kinematic indicators shows a consistent top-to-the-SSE sense of shear (51 out of 55).

Several brittle normal faults cut the shear-zone related structures (Fig. 3d). The late normal faults are more widespread along the coast line where they cut through the retrograde fabrics, but they

also occur locally inland. Along the coast most normal faults are S dipping, whereas further inland an antithetic N-dipping fault set occurs as well. Fault-slip analysis indicates that the normal faults also resulted from NW-SE extension (Fig. 5).

5. Finite-strain data and vorticity analysis

5.1. Finite strain

The finite-strain data are shown in Fig. 6. Most strain ellipsoids have an oblate symmetry (14 samples), but 2 have prolate symmetries and one sample plots near the plane-strain line. The scatter in strain symmetry indicates that deformation in the shear zone was heterogeneous. The most extremely deformed samples are characterized by upper/mid greenschist-facies deformation and usually have strong oblate symmetry with pronounced extension in the Y direction. Those samples are from the deep parts of the SSZ. There is a tendency for lower greenschist-facies samples to provide weakly oblate and prolate strain geometries.

We have not much control on possible volume changes associated with the accumulation of finite strain. However, the mylonitic granites do not show any signs of significant volume change within

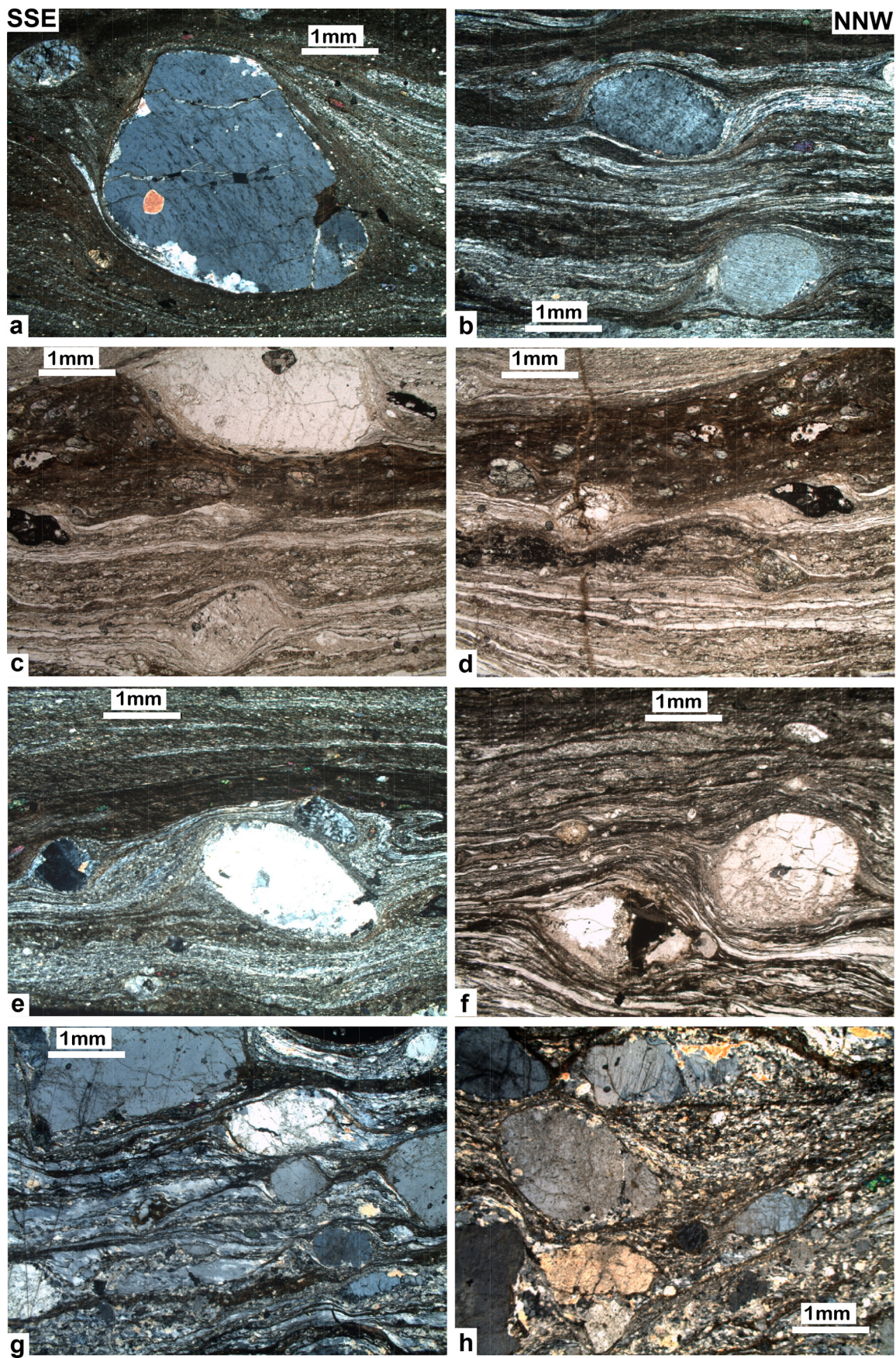


Fig. 4. Thin section photographs; SSE in all photos to left, scale bar represents 1 mm (refer to Fig. 2 for localities of samples). (a) Rounded potassium feldspar porphyroclasts with asymmetric tails indicative of top-to-the-SSE shear sense; sample SI9, South Arm. (b) Asymmetric tails around potassium feldspar indicating top-to-the-NNW sense of shear; sample SI10, South Arm. (c) Top-to-the-SSE and top-to-the-NNW shear sense in sample SI10. (d) Shear bands and asymmetric porphyroclasts indicating top-to-the-SSE shear sense; sample SI10. (e) Top-to-the-NNW shear sense indicated by asymmetric porphyroclast tails and microfolds; sample SI9. (f) Top-to-the-SSE sense of shear in sample SI-X. (g) Very thin retrograde shear bands made up by chlorite and Fe hydroxides supplying top-to-the-SSE shear sense; sample SI12. (h) Thin shear bands filled by Fe hydroxide and minor chlorite providing retrograde top-to-the-SSE sense of shear; sample SI11.

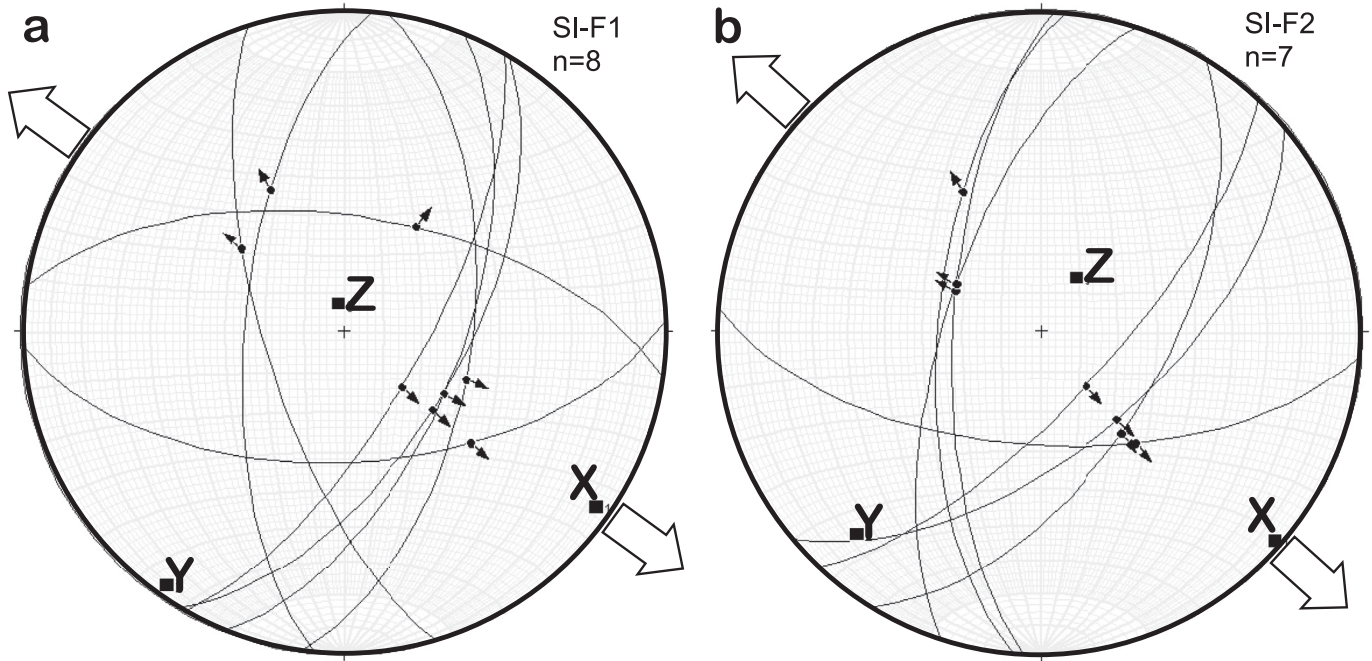


Fig. 5. Fault slip analysis of outcrops SI-F1 and SI-F2. Both outcrops characterised by conjugate NE- and NW-striking normal faults and supply NW-SE extension.

the SSZ. The blackish colour of ultramylonitic granite results from extreme deformation-related grain-size reduction and not from silica loss typical for volume deficient shear zones (Ring, 1999). We therefore assume volume-constant deformation, in which case the oblate strain geometry reflects a true flattening deformation.

A flattening strain geometry means that there are two principal extension directions in the SSZ. In other words, crustal extension was not by two-dimensional simple-shear deformation, which is a plane strain. The greatest amount of extension was in the SSE direction parallel to the stretching lineation mapped in the field. However, there was additional principal extension in the Y direction in the ENE direction. Below we report the results of a vorticity analysis that helps to quantify the coaxial component of deformation, which was caused by vertical flattening perpendicular to the shear zone walls.

5.2. Vorticity analysis

Ten mylonite samples from the SSZ were analysed using the PAR (4 samples, Fig. 7) and the PHD (6 samples, Fig. 8) methods. The mylonitic foliation served as the reference frame for analysis. For samples SI9 and SI10 the orientations of syn- and antithetic shear bands in the respective outcrops were measured as well and supplied W_m of 0.12 and 0.17, respectively. Overall, mean kinematic vorticity numbers range from $W_m = 0.10$ to $W_m = 0.89$ indicating significant heterogeneity of deformation and a distinct component of pure shear (Fig. 9).

Samples from the coast provide the highest W_m values (usually >0.71) and those from South Arm yielding values <0.2 (Fig. 9a). High W_m (>0.71) correlates with low d and R_{XZ} , whereas the samples with a very high pure-shear component have the highest strain intensity (Fig. 9b, c). In other words, samples from the low

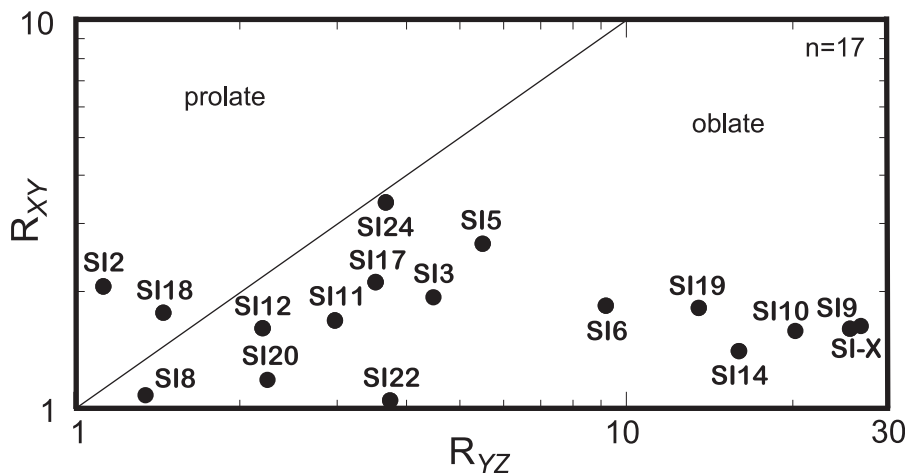


Fig. 6. Finite-strain data from SSZ plotted in strain symmetry diagram. Most data points lie in oblate field.

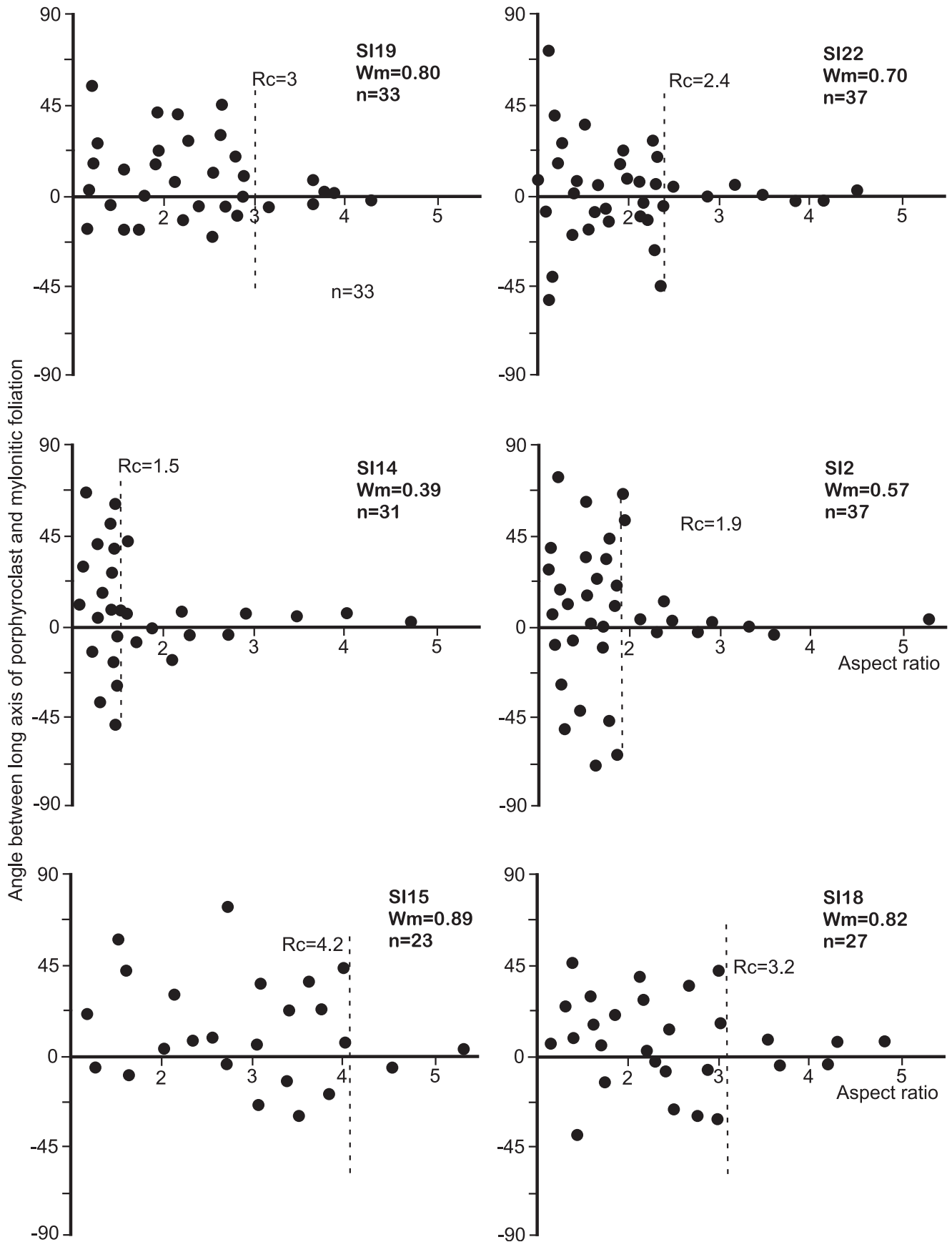


Fig. 7. Aspect ratios versus rotation angles of feldspar grains (PAR analysis); sample number, derived W_m and number of measured porphyroclasts indicated in upper right; dashed lines define critical aspect ratios (R_c), which divide objects whose long axes reached stable position subparallel to foliation and those with lower aspect ratios that rotated freely and show large scatter in orientations of long axes. For sample localities refer to Fig. 2.

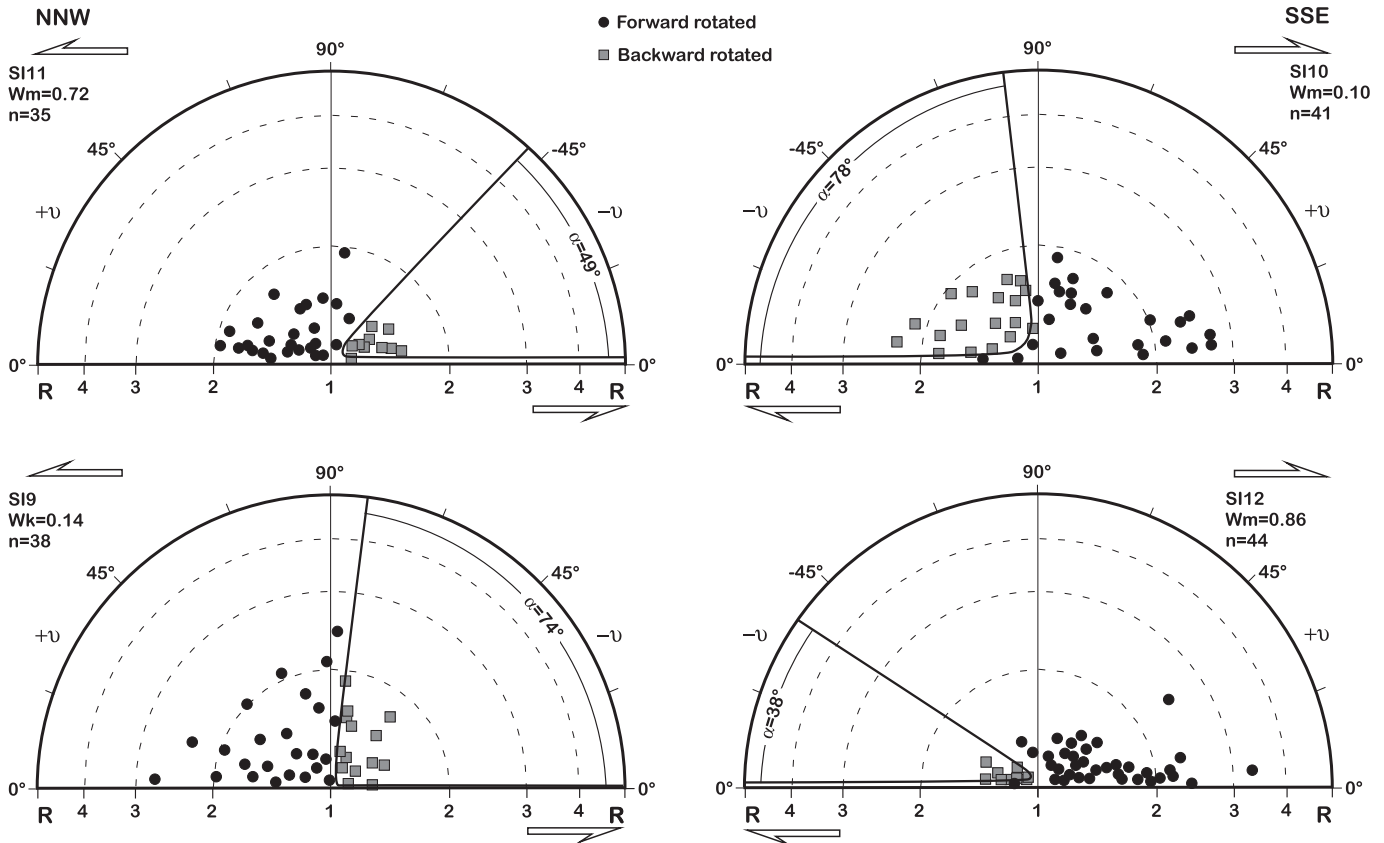


Fig. 8. PHD diagrams for mylonitic rocks; sample number, derived W_m and number of measured porphyroclasts indicated at top; porphyroclast axial ratios, R , are plotted against angle ν ; black circles represent forward-rotated porphyroclasts while grey-filled circles depict backward-rotated porphyroclasts; hyperbolas with interlimb angles provide W_m . For sample localities refer to Fig. 2.

greenschist-facies structurally high parts of the SSZ have lower strain magnitude and are characterized by a stronger simple-shear component than samples from structurally deep parts of the shear zone. The correlation between strain symmetry and structural position is relatively weak (Fig. 9d). When compared with the finite-strain symmetry, samples with strong flattening strain type tend to correlate with small $W_m \leq 0.2$ (Fig. 9b, c).

6. Apatite fission-track data and time-temperature history modelling

6.1. Apatite fission-track ages

The AFT ages are shown in Table 1. Most samples pass the chi-square test, but track counts are overall low, and as a consequence chi-square values may be upward biased. For eight samples we could measure tracks lengths, but the number of available confined horizontal tracks was rather limited (2–44 per sample). For those grains where tracks-lengths were measured Dpar values were also determined, which range between 1.74 and 2.36 μm (Table 2).

6.2. Comparison with other age data

Kula et al. (2007, 2009) reported $^{40}\text{Ar}/^{39}\text{Ar}$ muscovite ages from three samples (92.9–93.8 Ma), $^{40}\text{Ar}/^{39}\text{Ar}$ biotite ages from seven samples (86.6–94.6 Ma) and $^{40}\text{Ar}/^{39}\text{Ar}$ feldspar ages from five samples (85–112 Ma) and interpreted their ages as cooling ages. From a single sample in central Stewart Island Reiners et al. (2004) reported a single $^{40}\text{Ar}/^{39}\text{Ar}$ K-feldspar age spectrum, and zircon,

apatite and titanite (U-Th)/He ages of 76.8–87.6 Ma, 54.5–60.4 Ma and 85.4–92.7 Ma, respectively (Fig. 2). Overall, all ages suggest that the main activity of the SSZ was around 85–80 Ma.

6.3. Time-temperature history modelling

For samples P52239, P57396, P68117, SI06-3, SI06-15 and SI06-21 we determined time-temperature (t-T) histories (Fig. 10; Table 3) with HeFTy version 1.8.3. We use the $^{40}\text{Ar}/^{39}\text{Ar}$ age data of Kula et al. (2009) to constrain our t-T models. We also used the comprehensive (U-Th)/He data set of Reiners et al. (2004). However, the latter data come from an area about 10 km NNE of the SSZ. Assuming a closure temperature of 200 °C for titanite, 175 °C for zircon and 70 °C for apatite He ages.

The cooling history of our t-T models starts at 180 °C \pm 20 °C at 83 \pm 3 Ma for all samples, except sample SI06-15, for which a starting time of 76 \pm 3 Ma was selected. All thermal histories show fast cooling at ~85–80 Ma, with apparent rates of >50 °C Myr⁻¹ until about 80 Ma. Rapid cooling at about 80 Ma as derived by our t-T modelling from the SSZ is basically supported by similar titanite and zircon He ages from a pluton in central Stewart Island (Reiners et al., 2004). Apatite He ages of 55–60 Ma suggest slow cooling through temperatures of ~70 °C, which is consistent with our t-T models showing slow cooling after ~80 Ma at rates of the order of <5 °C after. No indication for reheating is observed. Consequently, this region has not experienced any heating since the late Cretaceous and has been cooling after early Cretaceous intrusions (Allibone and Tulloch, 1997, 2004) and extension across the SSZ (Kula et al., 2009).

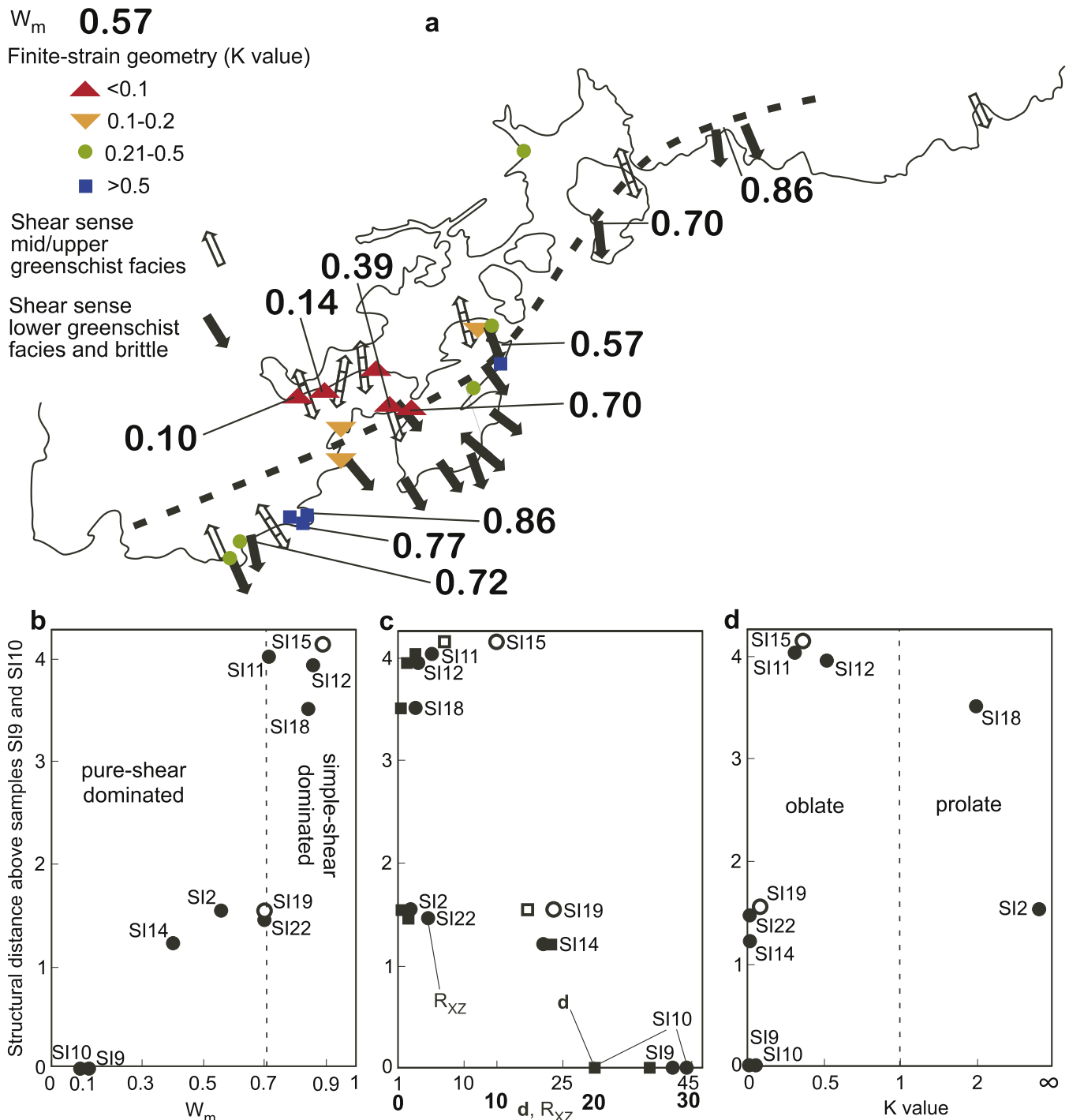


Fig. 9. (a) Summary map of SSZ showing W_m , K value and shear-sense data; dashed line separates upper SSZ characterized by $W_m > 0.71$, $K > 0.2$ and lower greenschist-facies top-to-the-SSE shear sense from deep SSZ in which $W_m < 0.71$, $K < 0.2$ and kinematic data do not provide consistent shear sense. (b–d) W_m , K value and strain intensity (d and R_{XZ}) as function of distance above structurally deepest samples SI9 and SI10; W_m shows increase in simple-shear component towards detachment, d and R_{XZ} decrease towards detachment; K shows weakest trend with slight increase in K towards detachment (samples SI15 and SI19 are from too far east to be projected into plot accurately and shown by hollow circles and squares).

7. Tectonic interpretation

7.1. Deformation regime in the SSZ

The maximum stretching direction during movement in the SSZ was NNW-SSE oriented and is reflected by the stretching lineations measured in the field (Kula et al., 2009; this study). Our data show

that deformation deviated significantly from progressive simple shear and involved a strong component of vertical flattening perpendicular to the shear zone walls. Associated with the general shear deformation are conflicting kinematic data showing alternating top-to-the-SSE and top-to-the-NNW senses of shear. Those conflicting kinematic data occur especially in the deep, upper greenschist-facies parts of the SSZ, where they are associated with

Table 1
Stewart Island apatite fission-track data.

Sample	n	ρ_s (10^{-5} cm $^{-2}$)	N_s	ρ_i (10^{-5} cm $^{-2}$)	N_i	ρ_d (10^{-5} cm $^{-2}$)	$P(\chi^2)$	Age (Ma)*	$\pm 1 \sigma$	U (ppm)	$\pm 1 \sigma$
SI06-1	15	2.73	(224)	3.33	(273)	5.38	60.2	63.9	6.8	9	1
SI06-2	15	3.26	(227)	3.16	(220)	5.37	99.6	80.0	8.6	9	1
SI06-3	15	9.48	(713)	9.85	(741)	5.36	17.7	75.2	5.9	28	2
SI06-5	15	3.33	(348)	3.64	(381)	5.35	100.0	70.7	6.4	10	1
SI06-6	15	2.54	(242)	2.58	(246)	5.34	89.4	76.0	7.9	7	1
SI06-8	15	2.00	(232)	1.82	(212)	5.34	34.6	84.4	9.4	5	1
SI06-10	14	2.21	(181)	2.27	(186)	5.33	56.0	75.0	8.7	6	1
SI06-13	15	7.57	(616)	7.71	(627)	5.32	97.6	75.6	5.8	22	2
SI06-15	15	4.63	(573)	4.73	(585)	5.31	74.5	75.3	5.9	13	1
SI06-16	15	5.25	(504)	5.08	(487)	5.06	29.6	75.7	6.6	15	1
SI06-17	15	4.39	(510)	4.21	(489)	5.30	2.1	81.0	8.0	12	1
SI06-18	15	2.73	(283)	2.24	(232)	5.29	63.2	93.2	9.5	6	1
SI06-19	12	2.00	(167)	1.34	(112)	5.28	91.3	113.6	15.0	4	1
SI06-20	15	2.73	(326)	3.04	(363)	5.28	37.3	68.8	6.5	9	1
SI06-21	14	9.17	(1066)	9.23	(1072)	5.27	0.1	75.3	6.4	26	2
P52239	15	8.61	(1008)	7.69	(900)	5.22	15.9	84.4	5.9	22	2
P57396	15	10.37	(1684)	13.9	(1704)	5.20	2.0	73.6	5.0	40	2
P59387	15	5.02	(542)	3.78	(408)	5.21	30.2	99.9	8.3	11	1
P63568	15	3.87	(376)	4.23	(411)	5.26	14.2	70.3	6.6	12	1
P63571	15	4.07	(260)	4.22	(270)	5.25	96.0	73.2	7.4	12	1
P63952	15	1.56	(182)	1.30	(152)	5.23	92.8	90.5	11.0	4	1
P63988	15	2.16	(251)	2.21	(257)	5.24	98.4	74.0	7.6	6	1
P68117	15	2.45	(295)	2.25	(271)	5.22	52.3	81.9	8.4	6	1

Note: Fission-track age is given as Central Age (Galbraith and Laslett, 1993). Samples were counted dry with a BH-2 Olympus microscope at 1250 \times magnification. Ages were calculated with the BINOMFIT program using a zeta value of 290.89 ± 14.49 (Bernet) and the IRMM540 uranium glass standard (15 ppm U).

very low kinematic vorticity numbers and strongly flattened strain geometry. The shear-sense indicators in the low greenschist-facies upper parts of the SSZ are uniformly top-to-the-SSE, finite strain is of weakly flattening type and deformation is dominated by a simple-shear component ($W_m > 0.71$). The top-to-the-SSE kinematic indicators formed in part in chloritic breccia and are assumed to have originated near the actual detachment surface (see also Kula et al., 2009).

Our quantitative data allow new interpretations of the architecture of the SSZ and the Great South Basin (Fig. 11). We emphasize that our interpretations have been aided by quantitative strain and rotation data. These data do not support a top-to-the-NNW (simple) shear zone in the southwest part of the SSZ as advocated by Kula et al. (2009, Fig. 11). The data are also not in line with significant along-strike differences in the kinematics of the SSZ (Kula et al., 2009). We interpret our strain and rotation data to provide a relatively uniform along-strike evolution of the shear zone. Given that the thermal regime during extension also does not show any significant variation along the strike of the SSZ, our findings are in line with the numerical modelling results of Gessner et al. (2007), which would predict a monovergent nature of the fairly low-grade Pegasus core complex. However, the data show marked heterogeneity in deformation, especially perpendicular to the shear zone.

In an extensional regime the maximum shortening direction is subvertical and subparallel to the vertical stress, the latter of which

is controlled by the thickness (z) and density (ρ) of the overburden ($\sigma_v = \rho gz$, where g = acceleration of gravity). For the deep parts of the SSZ syndeformational temperatures are assumed to be ≥ 450 °C, whereas the parts close to the detachment may record ~ 250 – 300 °C. Assuming a paleothermal gradient of 30° km $^{-1}$ during extension and an average rock density of 2800 kg m $^{-3}$ results in $\sigma_v \sim 0.23$ – 0.28 GPa near the detachment and $\sigma_v \geq 0.42$ GPa in the deep parts of the SSZ. In other words, σ_v near the detachments is > 30 – 40% less than at the bottom of the SSZ. We argue that the greater σ_v in the deep SSZ caused significant shortening perpendicular to the SSZ resulting in higher strain at the bottom of the shear zone (Fig. 9c). An additional factor might be that the higher-T structures formed over longer periods of time. Note that at least locally high-T structures were overprinted by lower-T ones and therefore more finite strain could accumulate in the high-T fabrics.

Associated with the high deformation intensity are low kinematic vorticity numbers (Fig. 9b) and sense of shear indicators at the bottom of the SSZ are top-to-the-SSE and top-to-the-NNW, respectively. Further up in the SSZ near the detachment separating the metamorphic core from the Great South Basin the sense of shear is more uniformly top-to-the-SSE. We explain the latter with a localisation of the simple-shear component of deformation in the uppermost shear zone near the detachment surface resulting in partitioning of the noncoaxiality of shear deformation (Fig. 11).

There is also a trend that the pronounced downward increase in strain magnitude correlates with an increased pure-shear flattening component (Fig. 9d). However, this trend is weak and sample SI2 with the highest K value of 8.7 has a low strain magnitude and a pure-shear dominated W_m (Fig. 9). It therefore seems that a correlation between the strain symmetry with respect to structural position and also relative to W_m and strain intensity is problematic. In general, strain symmetry is oblate and local deviations from the oblate strain symmetry may reflect flow heterogeneities during shearing deformation.

Despite the rather pronounced flattening component deep within the SSZ, the stretching lineations show a strong preferred orientation and not an additional stretching lineation parallel to the

Table 2
Stewart Island apatite fission-track lengths and Dpar.

Sample	Age (Ma)	$\pm 1 \sigma$	U (ppm)	$\pm 1 \sigma$	n	Mean length (μ m)	$\pm 1 \sigma$	Mean Dar (μ m)
SI06-3	75.2	5.9	28	2	40	13.39	0.21	2.31
SI06-13	75.6	5.8	22	2	2	13.16	0.26	2.36
SI06-15	75.3	5.9	13	1	28	13.33	0.25	2.04
SI06-20	68.8	6.5	9	1	5	8.47	1.27	1.76
SI06-21	75.3	6.4	26	2	28	13.03	0.26	1.99
P52239	84.4	5.9	22	2	15	13.67	0.26	1.74
P68117	81.9	8.4	6	1	27	13.12	0.38	1.90
P57396	73.6	5.0	40	2	44	13.53	0.23	2.21

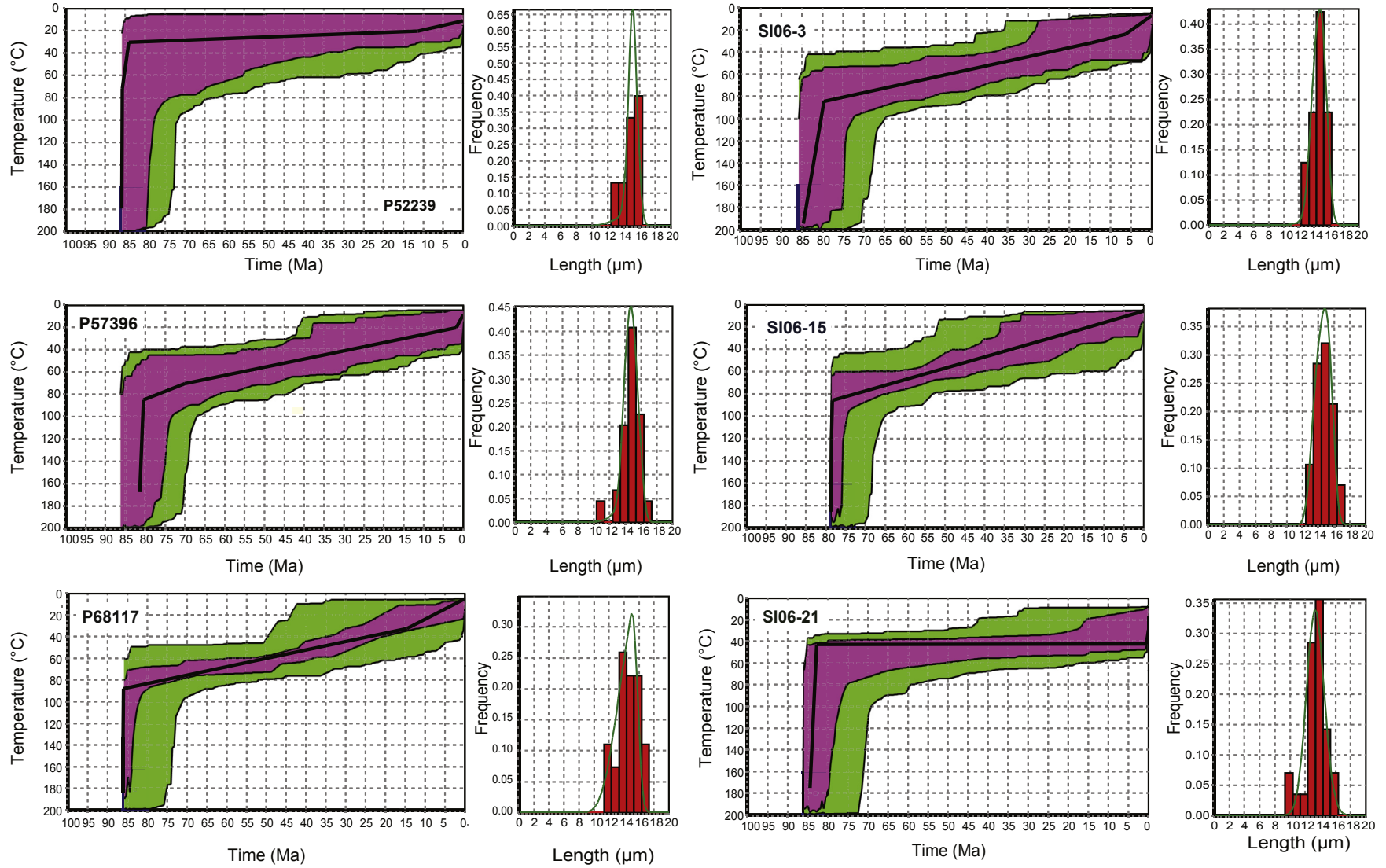


Fig. 10. Thermal history modelling using HeFTy version 1.8.3 (June 2014). Good-fit solution envelopes shown in magenta and acceptable-fit solution envelopes shown in green, black line is best-fit line. Observed AFT track-length distributions presented in histogram form, while modelled track-length distributions shown in curve form. (For interpretation of the references to color in this figure legend, the reader is referred to the web version of this article.)

Table 3
Stewart Island HeFTy Inversion modeling solutions.

Sample	Good fits	Acceptable fits	AFT model age (Ma)	GOF	AFT model track length (μm)	GOF
SI06-3	1174	4408	74.6	1.00	14.71 \pm 0.95	0.96
SI06-15	111	3877	72.8	0.59	14.73 \pm 0.98	0.93
SI06-21	357	4739	77.1	0.99	13.54 \pm 1.12	0.87
P52239	3916	5816	84.5	1.00	15.14 \pm 0.59	1.00
P68117	33	2434	76.5	0.48	14.37 \pm 1.07	0.86
P57396	1718	3975	74.3	0.99	14.62 \pm 0.88	1.00

Note: All solutions are based on 100,000 paths tried inverse modeling runs. GOF = Goodness of fit.

Y direction or a radial pattern. Ring (1999) showed for Proterozoic shear zones in East Africa that the orientation of stretching lineations in subhorizontal shear zones always maintain a strong maximum parallel to the tectonic transport direction despite low kinematic vorticity numbers. However, stretching lineations tend to show spatially heterogeneous bi-directional patterns in strike-slip shear zones with low kinematic vorticity numbers (Ring, 1999).

Our quantitative data are also important for studies in other large-scale shear zones. In line with many other studies (Grasemann et al., 1993; Simpson and De Paor, 1993; Northrup et al., 1996; Law et al., 2004; Kumerics et al., 2005; Bailey et al., 2007; Sullivan, 2008) our data show that progressive simple shear is a rather idealistic textbook concept that does often not seem applicable in the natural world. However, in a few cases shear regimes close to simple shear have been proven by quantitative data (Ring, 1998; Law et al., 2013). Another critical assumption commonly made, as in this study, is constant-volume deformation in shear zones.

Our main finding of a general shear deformation in the SSZ also has implication for the development of the Great South Basin. Given the flattening strain geometry it is conceivable that the perpendicular pattern of ENE- and NNW-striking faults may have resulted from the same late Cretaceous extension event and flattening strain was resolved in the basin above the Sisters Detachment by the formation of two orthogonal fault sets. The general shear deformation with pronounced vertical flattening leads to pronounced thinning of the shear zone and thus higher heat flow

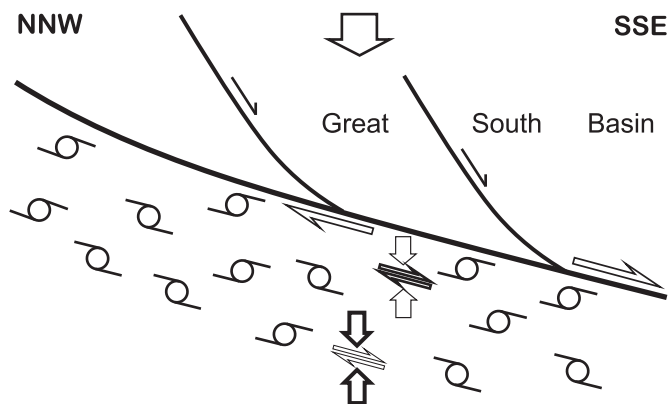


Fig. 11. Schematic section through Sisters Shear Zone and overlying Sisters Detachment illustrating envisaged deformation model based on shear-sense information, and strain and vorticity data. Shear-sense data from topmost footwall show consistent top-to-the-SSE displacement suggesting that rotational component of deformation was largely localised close to detachment. In deep SSZ shear-sense information is mixed and kinematic vorticity data indicate pure-shear dominated flow expressed by top-to-the-SSE and top-to-the-NNW displacement. We envisage that ENE- and NNW-striking faults in Great South Basin (Fig. 2) also result from pronounced vertical flattening during extension.

across it into the overlying sedimentary basin than the typical simple-shear type scenarios usually assumed for large-scale extensional tectonics. This has implications for models of hydrocarbon maturation and migration in the basin.

7.2. Thermal history

The AFT data and the t-T models show rapid cooling at 85–80 Ma. This rapid cooling is most likely related to tectonic exhumation during activity of the SSZ. The cooling ages just overlap with the age of the oldest sediments in the Great South Basin above the Sisters Detachment. It would follow that this stage of movement along the SSZ was the immediate precursor of Southern Ocean rifting at ~76 Ma (Gaina et al., 1998). The post-80 Ma cooling history of the SSZ samples is similar to the samples collected outside of the SSZ. This may indicate that post-80 Ma cooling was caused by slow regional erosional exhumation on the order of 0.1 km Myr⁻¹ or less.

Nonetheless, no ages for mylonitization and true higher temperature cooling ages (e.g. FT or (U-Th)/He on zircon, rutile or titanite) are available from the SSZ making it hard to compare footwall cooling of the Pegasus core complex to other core complex settings worldwide. In typical core complex settings like the Basin and Range province of the western US or the Aegean Sea rapid cooling at time-averaged rates exceeding 100 °C km⁻¹ from greenschist/amphibolite facies metamorphism is indicated by ages for mylonitization and zircon and apatite fission track cooling ages that are usually identical within error and of the same age as sediments in half graben in the hangingwall (Fitzgerald et al., 1991; Bryant et al., 1992; Foster and John, 1999; Kumerics et al., 2005; Brichau et al., 2006, 2007, 2010). At least the titanite and zircon (U-Th)/He ages of Reiners et al. (2004) from outside the SSZ are in the same range as the AFT ages from the SSZ, providing good evidence for rapid footwall cooling from ~200 °C at 85–80 Ma. It is conceivable that the GSB started to form by 100–95 Ma, in which case extensional deformation in the SSZ was either slow or involved two stages separated in time by 5–10 Myr. Mylonitization and higher temperature cooling ages in the footwall and more precise sedimentation ages in the hangingwall of the SSZ are needed to understand how footwall cooling relates to hangingwall sedimentation.

The high-angle normal faults are the only structures that can possibly be directly related to the AFT ages and the T-t paths. From a structural point of view the upper greenschist-facies structures resulted from the same general kinematics as lower greenschist-facies and brittle structures. This suggests kinematic coordination and that the structures formed during the same deformation event. If so, the higher-temperature structures would have also formed around 85 Ma or slightly earlier. However, this inference needs to be backed up by geochronologic data.

8. Conclusions

We have shown that the SSZ is a general shear zone whose kinematic development involved a significant component of pure shear flattening. The data show that only the upper SSZ near the Sisters Detachment had a significant simple shear component suggesting that the rotational component of shearing was partitioned into the detachment interface between foot- and hanging-wall. Our quantitative data also indicate along-strike kinematic continuity along the SSZ. The AFT ages and T-t models and the coherent kinematic evolution from upper greenschist-facies to brittle conditions suggest that the SSZ was active from >85 to 80 Ma.

Acknowledgements

We thank Virginia Toy and an anonymous reviewer for commenting on the manuscript and Joao Hippertt for editorial handling. Tulloch acknowledges research funding from the New Zealand Government.

References

- Allibone, A.H., Tulloch, A.J., 1997. Metasedimentary, granitoid, and gabbroic rocks from central Stewart Island, New Zealand. *N. Z. J. Geology Geophys.* 40, 53–68.
- Allibone, A.H., Tulloch, A.J., 2004. Geology of the plutonic basement rocks of Stewart Island, New Zealand. *N. Z. J. Geol. Geophys.* 47, 233–256.
- Allibone, A.H., Tulloch, A.J., 2008. Early Cretaceous dextral transpressional deformation within the median Batholith, Stewart Island, New Zealand. *N. Z. J. Geol. Geophys.* 51, 115–134.
- Bailey, C.M., Polvi, L.E., Forte, A.M., 2007. Pure shear dominated high-strain zones in basement terranes. *Geological Soc. Am. Mem.* 200, 93–108.
- Brandon, M.T., Roden-Tice, M.K., Garver, J.L., 1998. Late Cenozoic exhumation of the Cascadia accretionary wedge in the Olympic Mountains, northwest Washington State. *Geological Soc. Am. Bull.* 110, 985–1009.
- Brichau, S., Ring, U., Carter, A., Ketcham, R.A., Brunel, M., Stockli, D., 2006. Constraining the long-term evolution of the slip rate for a major extensional fault system using thermochronology. *Earth and Planetary Science Letters* 241, 293–306.
- Brichau, S., Ring, U., Carter, A., Monié, P., Bolhar, R., Stockli, D., Brunel, M., 2007. Extensional faulting on Tinos Island, Aegean Sea, Greece: how many detachments? *Tectonics* 26 (4), TC4009. <http://dx.doi.org/10.1029/2006TC001969>, 19 pages.
- Brichau, S., Thomson, S.N., Ring, U., 2010. Thermochronometric constraints on the tectonic evolution of the Serifos detachment, Aegean Sea, Greece. *Int. J. Earth Sci.* 99, 379–393. <http://dx.doi.org/10.1007/s00531-008-0386-0>.
- Bryant, B.C., Naeser, W.J., Fryxell, E., 1992. Implications of low-temperature cooling history on a transect across the Colorado Plateau-Basin and Range Boundary, west central Arizona, 96, 12375–12388. <http://dx.doi.org/10.1029/90JB02027>.
- Deckert, H., Ring, U., Mortimer, N., 2002. Tectonic significance of Cretaceous bivertent extensional shear zones in the Torlesse accretionary wedge, central Otago Schist, New Zealand. *N. Z. J. Geology Geophys.* 45, 537–547.
- Donelick, R.A., O'Sullivan, P.B., Ketcham, R.A., 2005. Apatite fission-track analysis. *Rev. Mineral. Geochem.* 58, 49–94. <http://dx.doi.org/10.2138/rmg.2005.58.3>.
- Ehlers, T.A., 2005. Crustal thermal processes and thermochronometer interpretation. *Rev. Mineral. Geochem.* 58, 315–350.
- Farley, K.A., 2000. Helium diffusion from apatite: general behavior as illustrated by Durango fluorapatite. *J. Geophys. Res.* 105, 2903–2914.
- Fitzgerald, P.G., Fryxell, J.E., Wernicke, B.P., 1991. Miocene crustal extension and uplift in southeastern Nevada: constraints from apatite fission track analysis. *Geology* 19, 1013–1016.
- Foster, D.A., John, B.E., 1999. Quantifying tectonic exhumation in an extensional orogen with thermochronology: examples from the southern Basin and Range Province. *Geol. Soc. Lond. Spec. Publ.* 154, 343–364. <http://dx.doi.org/10.1144/GSL.SP.1999.154.01.16>.
- Fry, N., 1979. Density distribution techniques and strain length methods for determination of finite strains. *J. Struct. Geology* 1, 221–229.
- Ghosh, S.K., Ramberg, H., 1976. Reorientation of inclusions by combination of pure shear and simple shear. *Tectonophysics* 34, 1–70.
- Gaina, C., Müller, D.R., Royer, J.-Y., Stock, J., Hardebeck, J., Symonds, P., 1998. The tectonic history of the Tasman Sea: a puzzle with 13 pieces. *J. Geophys. Res. – Solid Earth* 103, 12413–12433.
- Galbraith, R.F., Laslett, G.M., 1993. Statistical models for mixed fission track ages. *Nucl. Tracks Radiat. Meas.* 21, 459–470.
- Gessner, K., Wijns, C., Moresi, L., 2007. Significance of strain localization in the lower crust for structural evolution and thermal history of metamorphic core complexes. *Tectonics* 26, TC2012.
- Grasemann, B., Fritz, H., Vannay, J.C., 1999. Quantitative kinematic flow analysis from the main central thrust zone (NW-Himalaya, India): implications for a decelerating strain path and the extrusion of orogenic wedges. *J. Struct. Geology* 21, 837–853.
- Green, P.F., Duddy, I.R., Laslett, G.M., Hegarty, K.A., Gleadow, A.J.W., Lovering, J.F., 1989. Thermal annealing of fission tracks in apatite 4. Quantitative modelling techniques and extension to geological timescales. *Chem. Geol. Isot. Geosci. Sect.* 79 (2), 155–182.
- Hurford, A.J., Green, P.F., 1983. The zeta age calibration of fission-track dating. *Isot. Geosci.* 1, 285–317.
- Jeffery, G.B., 1922. The motion of ellipsoidal particles immersed in a viscous fluid. *Proc. R. Soc. Lond.* A102, 161–179.
- Kassem, O.K., Ring, U., 2004. Underplating-related finite-strain patterns in the Gran Paradiso massif, Italian Western Alps: heterogeneous ductile strain superimposed on a nappe stack. *J. Geol. Soc. Lond.* 161, 875–884.
- Ketcham, R.A., 2005. Forward and inverse modeling of low-temperature thermochronometry data. *Rev. Mineral. Geochem.* 58, 275–314. <http://dx.doi.org/10.2138/rmg.2005.58.11>.
- Ketcham, R.A., Carter, A., Donelick, R.A., Barbarand, J., Hurford, A.J., 2007. Improved modeling of fission-track annealing in apatite. *Am. Mineral.* 92, 799–810. <http://dx.doi.org/10.2138/am.2007.2281>.
- Ketcham, R.A., Donelick, R.A., Balestrieri, M.L., Zattin, M., 2009. Reproducibility of apatite fission-track length data and thermal history reconstruction. *Earth Planet. Sci. Lett.* 284, 504–515.
- Ketcham, R.A., Donelick, R.A., Carlson, W.D., 1999. Variability of apatite fission-track annealing kinetics; III, extrapolation to geological time scales. *Am. Mineral.* 84, 1235–1255.
- Kula, J., Tulloch, A.J., Spell, T.L., Wells, M.L., Zanetti, K.A., 2009. Thermal evolution of the Sisters shear zone, southern New Zealand: formation of the Great South Basin and onset of Pacific-Antarctic spreading. *Tectonics* 28, TC5015. <http://dx.doi.org/10.1029/2008TC002368>.
- Kula, J., Tulloch, A., Spell, T.L., Wells, M.L., 2007. Two-stage rifting of Zealandia-Australia-Antarctica: evidence from ⁴⁰Ar/³⁹Ar thermochronometry of the Sisters Shear Zone; Stewart Island, New Zealand. *Geology* 35, 411–414. <http://dx.doi.org/10.1130/G23432A.1>.
- Kumerics, C., Ring, U., Brichau, S., Glodny, J., Monié, P., 2005. The extensional Messaria shear zone and associated brittle detachment faults, Aegean Sea, Greece. *J. Geol. Soc. Lond.* 162, 701–721.
- Kurz, G.A., Northrup, C.J., 2008. Structural analysis of mylonitic fault rocks in the Cougar Creek Complex, Oregon-Idaho using the porphyroclast hyperbolic distribution method, and potential use of SC-type extensional shear bands as quantitative vorticity indicators. *J. Struct. Geol.* 30, 1005–1012.
- Law, R.D., Searle, M.P., Simpson, R.L., 2004. Strain, deformation temperatures and vorticity of flow at the top of the greater Himalayan Slab, Everest Massif, Tibet. *J. Geol. Soc. Lond.* 161, 305–320.
- Law, R.D., Stahr, D.W., Francis, M.K., Ashley, K.T., Grasemann, B., Ahmad, T., 2013. Deformation temperatures and flow vorticities near the base of the Greater Himalayan Series, Sutlej Valley and Shimla Klippe, NW India. *J. Struct. Geol.* 54, 21–53. <http://dx.doi.org/10.1016/j.jsg.2013.05.009>.
- Lister, G.S., Davis, G.A., 1989. The origin of metamorphic core complexes and detachment faults formed during tertiary continental extension in the northern Colorado River region, U.S.A. *J. Struct. Geol.* 11 (1–2), 65–94.
- Means, W.D., 1989. Stretching faults. *Geology* 17, 893–896.
- Mortimer, N., 1993. Jurassic tectonic history of the Otago schist, New Zealand. *Tectonics* 12, 237–244.
- Mortimer, N., 2004. New Zealand's geological foundations. *Gondwana Res.* 7, 261–272.
- Nathan, S., Rattenbury, M.S., Suggate, R.P., 2002. Geology of the Greymouth Area. Institute of Geological & Nuclear Sciences Geological Map 12. Scale 1:250 000. Institute of Geological & Nuclear Sciences, Lower Hutt, New Zealand.
- Northrup, C.J., 1996. Structural expressions and tectonic implications of general non-coaxial flow in the midcrust of a collisional orogen: the northern Scandinavian Caledonides. *Tectonics* 15, 490–505.
- Owens, W.H., 1984. The calculation of a best fit ellipsoid from elliptical sections on arbitrarily oriented planes. *J. Struct. Geol.* 6, 571–578.
- Passchier, C.W., 1987. Stable positions of rigid objects in non-coaxial flow: a study in vorticity analysis. *J. Struct. Geol.* 9, 679–690.
- Passchier, C.W., 1988. Analysis of deformation paths in shear zones. *Geol. Rundsch.* 77, 309–318.
- Platt, P.P., Vissers, R.L.M., 1980. Extensional structures in anisotropic rocks. *J. Struct. Geol.* 2, 397–410.
- Ramsay, J.G., Graham, R.H., 1970. Strain variation in shear belts. *Can. J. Earth Sci.* 7, 786–813.
- Ramsay, J.G., Huber, M.I., 1983. The techniques of modern structural geology. In: *Strain Analysis*, vol. 1. Academic Press.
- Rattenbury, M.S., 1991. The Fraser Complex: high-grade metamorphic, igneous and mylonitic rocks in central Westland, New Zealand. *N. Z. J. Geology Geophys.* 34, 23–33.
- Reiners, P.W., Spell, T.L., Nicolescu, S., Zanetti, K.A., 2004. Zircon (U-Th)/He thermochronometry: He diffusion and comparison with ⁴⁰Ar/³⁹Ar dating. *Geochimica Cosmochimica Acta* 68, 1857–1887.
- Ring, U., 1998. Strain geometry, flow path and volume deformation in a narrow shear zone. *Geol. Rundsch.* 86, 786–801.
- Ring, U., 1999. Volume loss, fluid flow and coaxial vs noncoaxial deformation in retrograde, amphibolite-facies shear zones, northern Malawi, east-central Africa. *Geol. Soc. Am. Bull.* 111, 123–142.
- Ring, U., Layer, P.W., Reischmann, T., 2001. Miocene high-pressure metamorphism in the Cyclades and Crete, Aegean Sea, Greece: evidence for large-magnitude displacement on the Cretan detachment. *Geology* 29, 395–398.
- Ring, U., Kumerics, C., 2008. Vertical ductile thinning and its contribution to the exhumation of high-pressure rocks: the Cycladic blueschist unit in the Aegean. *J. Geol. Soc. Lond.* 165, 1019–1030.
- Schulte, D.O., Ring, U., Thomson, S., Glodny, J., Carrad, H., 2014. Two-stage development of the paparoa metamorphic core complex, West Coast, South Island, New Zealand: hot continental extension precedes seafloor spreading by ~25 Myr. *Lithosphere* 6, 177–194. <http://dx.doi.org/10.1130/L348.1>.
- Spell, T.L., McDougall, I., Tulloch, A.J., 2000. Thermochronologic constraints on the breakup of the Pacific Gondwana margin: the Paparoa metamorphic core complex, South Island, New Zealand. *Tectonics* 19, 433–451.
- Simpson, C., De Paor, D.G., 1997. Practical analysis of general shear zones using the porphyroclast hyperbolic distribution method: an example from the Scandinavian Caledonides. In: Sengupta, S. (Ed.), *Evolution of Geological Structures in Micro- to Macro-scales*. Chapman and Hall, pp. 169–184.

- Simpson, C., De Paor, D.G., 1993. Strain and kinematic analysis in general shear zones. *J. Struct. Geol.* 15, 1–20.
- Sullivan, W.A., 2008. Significance of transport-parallel strain variations in part of the Raft River shear zone, Raft River Mountains, Utah, USA. *J. Struct. Geology* 30, 138–158.
- Thomson, S.N., Ring, U., 2006. Thermochronologic evaluation of post-collision extension in the Anatolide Orogen, western Turkey. *Tectonics* 25. <http://dx.doi.org/10.1029/2005 TC001833>, TC3005, 20p.
- Tulloch, A.J., Kimbrough, D.L., 1989. The paparoa metamorphic core complex, New Zealand: cretaceous extension associated with fragmentation of the Pacific margin of Gondwana. *Tectonics* 8, 1217–1234.
- Tulloch, A.J., Beggs, M., Kula, J.L., Spell, T.L., Mortimer, N., 2006. Cordillera Zealandia, the Sisters shear zone and their influence on the early development of the Great South Basin. Paper Presented at the New Zealand Petroleum Conference 2006, Crown Minerals, Auckland, New Zealand.
- Uruski, C., Ilg, B., 2006. Preliminary Interpretation and Structural Modelling of DUN06 Seismic Reflection Data from Great South Basin, Offshore New Zealand. GNS Science Consultancy, p. 46. Report 2006/233.
- Wells, M.L., Snee, L.W., Blythe, A.E., 2000. Dating of major normal fault systems using thermochronology: an example from the Raft River detachment, Basin and Range, western United States. *J. Geophys. Res.* 105, 16,303–16,327.
- Wolf, R.A., Farelly, K.A., Silver, L.T., 1996. Helium diffusion and low-temperature thermochronometry of apatite. *Geochimica Cosmochimica Acta* 60, 4231–4240.
- Xypolias, P., 2010. Vorticity analysis in shear zones: a review of methods and applications. *J. Struct. Geol.* 32, 2072–2092.